Roquin binding to target mRNAs involves a winged helix-turn-helix motif

Schuetz, A., Murakawa, Y., Rosenbaum, E., Landthaler, M., Heinemann, U.

This is the final version of the manuscript. The original article has been published in final edited form in:

Nature Communications
2014 DEC 11 ; 5: 5701
doi: 10.1038/ncomms6701
Publisher: Nature Publishing Group

Roquin binding to target mRNAs involves a winged helix-turn-helix motif

Anja Schuetz[1], Yasuhiro Murakawa[2], Eva Rosenbaum[3], Markus Landthaler[2] and Udo Heinemann[1,4]

[1] Helmholtz Protein Sample Production Facility, Max Delbrück Center for Molecular Medicine, Berlin, Germany

[2] Laboratory for RNA Biology and Posttranscriptional Regulation, Berlin Institute for Medical Systems Biology, Max Delbrück Center for Molecular Medicine, Berlin, Germany

[3] Structure and Membrane Interaction of G-Proteins, Max Delbrück Center for Molecular Medicine, Berlin, Germany

[4] Chemistry and Biochemistry Institute, Freie Universität Berlin, Berlin, Germany

Correspondence: Udo Heinemann

Abstract

Roquin proteins mediate mRNA deadenylation by recognizing a conserved class of stem-loop RNA degradation motifs *via* their roquin domain. Here, we present the crystal structure of a roquin domain, and by combining structural, biochemical and mutation analyses we gain insight into the mode of RNA binding. We show that the winged helix-turn-helix motif is involved in the binding of constitutive decay elements-containing stem-loop mRNAs. Moreover, we provide biochemical evidence that roquin proteins are additionally able to bind to duplex RNA and have the potential to be functional in different oligomeric states.

Introduction

Binding of proteins to distinct *cis*-regulatory elements within the untranslated region (UTR) of messenger RNAs (mRNAs) regulates the lifespan of these mRNAs and controls gene expression at the posttranscriptional level. Roquin proteins, for example, were recently reported to specifically bind to a newly discovered conserved class of RNA stem-loop motifs, known as constitutive decay elements (CDE), that are present in the 3' UTR of various mRNAs, thereby initiating their degradation. On a transcriptome-wide scale, more than 50 vertebrate CDE-containing mRNAs were identified as Roquin targets, many of which encode proteins important for development as well as inflammation and immunity[1]. Roquin binding to the CDE in the 3' UTR of tumor necrosis factor-α (TNF-α) mRNA, for example, limits the synthesis of the pro-inflammatory cytokine TNF-α[1]. The expression of *ICOS* (inducible T-cell co-stimulator), a gene encoding an essential receptor for follicular T-cells, is also restricted by Roquin, which promotes the degradation of ICOS mRNA, thereby playing an important role in autoimmunity[2,3].

Mammalian genomes encode two roquin paralogs with seemingly redundant functions[4,5]. Human ROQUIN1, also known as RC3H1 (ring finger and CCCH-type zinc finger domains 1), is a 1,133 amino-acid protein, containing a RING (really interesting new gene)-type zinc finger, a roquin domain (ROQ), a CCCH-type zinc finger (zf), and a poorly defined C-terminal, proline-rich domain. Murine Roquin binding to CDE-like RNA stem-loop motifs was shown to be mediated by the ROQ domain, while the C-terminal effector domain recruits the Ccr4-Caf1-Not complex, resulting in Caf1a-dependent deadenylation and consecutive degradation of CDE-containing mRNAs[1]. Although Roquin proteins were shown to act broadly as mediators of mRNA deadenylation by recognizing a conserved class of stem-loop RNA degradation motifs *via* the ROQ domain[1], the structural basis for stem-loop mRNA recognition is still unknown. To shed light on this, we determined the crystal

structure of the ROQ domain of the human ROQUIN1 protein revealing a wHTH motif. Additional biochemical and mutational analyses show that ROQUIN1 is able to bind both stem-loop and duplex RNA and that these interactions are mediated by the wHTH motif. Moreover, we provide evidences that ROQUIN1 has the potential to be functional in various oligomeric states and also provide a dimer model of the ROQ domain.

Results

Crystal structure of the ROQ domain

To obtain the crystal structure of the human ROQUIN1/RC3H1 protein, several constructs were used for crystallization. Although the produced proteins comprised up to three functional domains (RING, ROQ, zf domains), we always obtained the same degradation product, most likely representting the ROQ domain with all stably folded elements. We determined the crystal structure of this portion of ROQUIN1 at 1.91-Å resolution by SAD phasing. The final model was refined to an R_{work} of 20.0% and an R_{free} of 24.1% (**Table 1**, **Supplementary Fig. 1a-b**) and includes amino-acid residues 177 to 328. The overall structure of the ROQ domain shows a compact (α+β) fold featuring seven α-helices, one 3_{10}-helix and a short three-stranded antiparallel β-sheet (**Fig. 1a**). The structure reveals a winged helix-turn-helix (wHTH) motif spanning from helix α2 to the 3_{10}-helix η1, with helix α1 and helices α5-α7 from the ROQ domain packing against the wHTH motif (**Fig. 1a-b, Supplementary Fig. 1a**). The overall fold is stabilized by a salt bridge between the wHTH motif (R251 in helix α4) and a C-terminal residue of helix α5 (E293), and by hydrogen bonding interactions between the N-terminal helix α1 and helices α2 and α4 of the wHTH motif.

The canonical wHTH motif has originally been described to bind double-stranded DNA and consists of three α-helices (H1-H3), three β-strands (S1–3) and two characteristic loops ('wings') W1 and W2, arranged in the order H1-S1-H2-H3-S2-W1-S3-W2[6]. Notably, in the crystal structure of the ROQ domain, the wHTH motif adopts a similar conformation with the exception that the W2-loop of the canonical wHTH motif is folded into the single-turn 3_{10}-helix η1 (**Fig. 1a-b**). Moreover, the putative RNA-binding pocket is located within the wHTH motif as illustrated by electrostatic potential mapping (**Fig. 1c**).

Currently, the wHTH motif is described as a conserved structural element whose interaction profiles and functional properties in different proteins are extremely versatile, ranging from nucleic-acid binding to protein-protein interactions[6]. Search for structural homologs using the DALI server[7] and PDBeFold[8] returned no matches for the entire structure but to other wHTH-containing protein domains, whereby sharing a sequence identity of only 10-15%, explaining the missed wHTH motif prediction. The DNA replication factor Cdt1 (PDB code 3a4c[9]), a key licensing factor which recruits the MCM2-7 complex onto the origin of chromosomes, is the closest structural homolog with a root-mean-square deviation (rmsd) of 3.2 Å over 99 α-carbons (**Supplementary Fig. 2a**). Other structural similarity matches identified by the DALI[7] search were to wHTH domains found in E3-ubiquitin-ligase complexes. The complex of the C-terminal domain of cullin-1 and the RING domain of the E3-ubiquitin ligase Rbx1[10], for example, superimposes with an rmsd of 3.8 Å over 79 residues onto the wHTH motif of the ROQ domain (**Supplementary Fig. 2b**). In the cullin-RING ligase complex, the wHTH subdomain of cullin-1 mediates contacts with the Rbx-1 RING domain, and similar interactions might be observed between the wHTH motif of the ROQ domain and the N-terminal RING domain of ROQUIN1.

Notably, no matches to other proteins with classical wHTH motifs and reported RNA-binding properties were found among the top hits in the structural similarity search[7]. However, to date only few such proteins have been described, displaying diverse RNA recognition modes[11-16]. Among these, the selenocysteine tRNA-specific elongation factor SelB is the single example of a wHTH-containing protein recognizing stem-loop mRNA. Its C-terminal domain encompasses four wHTH domains. The two terminal tandem wHTH motifs synergize to establish specific interactions with the selenocysteine incorporation site (SECIS) hairpin, and the last motif specifically recognizes the mRNA-specific hairpin tip structure of the mRNA[12,16]. The C-terminal SelB wHTH domain superimposes with an rmsd of 3.1 Å over 73 residues onto the wHTH motif within the crystal structure of the ROQ domain, displaying a similar electropositive pocket as described for the ROQ domain crystal structure (**Supplementary Fig. 2c**).

ROQUIN1 binding to CDE-containing stem-loop mRNAs

Structural analysis indicated a role of the wHTH motif of the ROQ domain in RNA binding. To support this finding, we analyzed the RNA-binding properties of different wHTH variants. Within the wHTH motif, single basic residues that may confer binding of the RNA backbone are highly conserved throughout the roquin homologs. However, clusters of basic solvent-accessible residues can be found at the N-terminal base of helix α3 (R219 and K220) and in the β2-β3 loop (K259 and R260) (**Supplementary Fig. 3**). To verify a potential involvement of these wHTH residues in mRNA binding, we performed electrophoretic mobility shift assays (EMSA) using wild-type and variant proteins comprising the RING, ROQ and zf domains of ROQUIN1 ($RC3H1^{2-452}$), and the isolated CDE-containing stem-loop structure of ICOS mRNA. Wild-type $RC3H1^{2-452}$ binds with a K_d value of 139 ± 42 nM to ICOS stem-loop mRNA (**Fig. 2a**), which is comparable to the binding

constant reported for another CDE-containing stem-loop mRNA, namely TNF-α (92 ± 14 nM)[1]. On the other hand, RC3H1$^{2-452}$ variants with single basic patch mutations (RK219AA or KR259AA, respectively) showed significantly reduced ICOS binding while simultaneous mutation of the two basic patches nearly abolished binding (**Fig. 2a**), clearly demonstrating an involvement of the wHTH motif in stem-loop mRNA binding. Notably, the observed effects are not due to altered secondary structures induced by the mutation as demonstrated by circular dichroism spectroscopy (CD) measurements (**Supplementary Fig. 4**).

Stem-loop RNA binding to dimeric ROQUIN1

ROQUIN1 purified as monomeric protein as judged by its gel filtration profile. To verify the oligomerization state in solution, we additionally performed sedimentation velocity ultra-centrifugation experiments with the RC3H1$^{2-452}$ protein, revealing the presence of 60% monomers, 33% dimers, and 7% higher oligomers (**Fig. 2b**). This points towards the ability of ROQUIN1 to bind to RNA in various oligomerization states. To shed light on this, we next repeated the experiment in the presence of stem-loop ICOS RNA. All protein peaks are shifted to higher sedimentation coefficients upon complex formation with RNA with no significant changes in the relative abundance of the various species, supporting the above hypothesis (**Fig. 2b**).

Analysis of the analytical ultracentrifugation experiments indicated that, in addition to monomeric protein, also ROQUIN1 dimers are able to bind to stem-loop RNA. Inspection of the ROQ domain crystal structure and adjacent symmetry-related segments by using ePISA[17] revealed a potential dimer arrangement (**Fig. 3a**) that could allow for independent binding of two stem-loop RNA molecules to the two electropositive wHTH sites within the dimer (**Fig. 3b**), assuming that the stem-loop RNA binding sites are identical in monomeric and dimeric ROQUIN1. Moreover, we consider

this crystallographic dimer rather weak *per se* as indicated by the small buried surface area of 738 $Å^2$ with a limited number of hydrogen bonding and salt-bridge interactions at the dimer interface (**Supplementary Table 1**), and the fact that the dimeric fraction of uncomplexed ROQUIN1, whose existence has been indicated by our analytical ultracentrifugation experiments (**Fig. 2b**), is not stable under the separation shear forces on a gel filtration (**Supplementary Fig. 5a**).

To verify that this proposed dimer is capable of stem-loop RNA binding, we designed a dimer-stabilizing mutant and introduced two disulfide bridges at the dimer interface by generating the P327C/T258C variant, which links the C-terminus of the ROQ domain to the C-terminal end of β2 within the wHTH motif. The double cysteine variant purifies as a mixture of monomers and dimers, with the dimeric fraction being convertible to monomers upon DTT treatment (**Supplementary Fig. 5b**) and with a secondary-structure content similar to wild-type protein (**Supplementary Fig. 4**). Strikingly, the disulfide-stabilized dimer possesses a significantly increased stem-loop RNA affinity compared to wild-type protein as revealed by EMSA (**Fig. 3c**). Addition of DTT brings the RNA binding ability back to wild-type level (**Fig. 3c**), supporting our proposed dimer model.

ROQUIN1 binding to duplex RNA

To further analyze the stoichiometry of RNA binding to ROQUIN1, we performed isothermal titration calorimetry (ITC) where we calculated an unexpected overall binding stoichiometry of around 0.5, implying that two molecules of $RC3H1^{2-452}$ protein bind to one molecule of RNA (**Fig. 3d**). However, we realized that the concentrations applied during this ITC experiment involved RNA annealing at a rather high concentration yielding bulged duplex RNA instead of the stem-loop form (**Supplementary Fig. 5c, Supplementary Fig. 6**), a phenomenon that has also been described by Tan *et al.*[18]. Interestingly, we determined a K_d value of 68.9 ± 8.6 nM for the binding of $RC3H1^{2-}$

^{452} to ICOS duplex RNA (**Fig. 3d**), which is in the same range as observed for stem-loop RNA. Taken together, ROQUIN1 is not only able to bind to stem-loop but also to double-stranded RNA.

Results from analytical gel filtration experiments confirmed the 2:1 binding model indicated by the above ITC experiment. In the absence of duplex RNA, the calculated molecular mass corresponds to monomeric RC3H1$^{2-452}$ protein, and dimeric protein was found in the presence of duplex ICOS RNA (**Supplementary Fig. 5a**). Notably, we observe a complete shift of the monomeric fraction upon duplex RNA addition despite adding only 0.6-fold molar amount of duplex RNA to prepare the complex. The same holds true also for the crystallized RC3H1$^{178-328}$ degradation fragment of ROQUIN1, indicating that the RING and zf domains of ROQUIN1 are dispensable for both RNA binding and dimerization (**Supplementary Fig. 5d**).

The latter finding hints towards the possibility that the proposed ROQ domain dimer arrangement (**Fig. 3a**) may also support duplex RNA binding. In accordance with the 2:1 binding stoichiometry and the electrostatic potential mapping (**Fig. 3b**), the putative duplex RNA binding site is likely located at the dimer interface. Furthermore, the width of the binding groove at the dimer interface seems sufficient to accommodate double-stranded RNA. To prove our hypothesis, we performed an ITC experiment using the cysteine-bridged P327C/T258C variant of RC3H1$^{2-452}$. Remarkably, a ROQUIN1 dimer stabilized this way binds to ICOS duplex RNA with the same 2:1 stoichiometry as described before (when referring to monomer protein in ITC calculations), substantiating the dimer model (**Fig. 3d**). The, compared to wild-type, observed about 10-fold decreased K_d value for duplex ICOS binding to the stabilized ROQUIN1 dimer variant may be attributed to the decrease of flexibility in the rigidified cysteine-bridged dimer, which otherwise may be necessary for efficient duplex RNA binding at the dimer interface (**Supplementary Fig. 7a**).

Since the two basic patches within the wHTH motif contribute to the electropositive surface at the dimer interface, we next tested whether a variant with simultaneous mutation of these sites (RK219AA and KR259AA) would also interfere with duplex ICOS binding. Indeed, this variant nearly abolished duplex RNA binding (**Supplementary Fig. 8**), demonstrating that the wHTH motif within the ROQ domain is not only involved in stem-loop RNA binding but also has the potential to recognize double-stranded RNA.

Last, we examined whether the ROQ-domain dimerization is mediated predominantly by duplex RNA binding or by monomer-monomer contacts. ITC experiments show that the RC3H1$^{2\text{-}452}$ variant proteins bearing mutations in the dimer interface bind double-stranded ICOS RNA with similar affinity as wild-type ROQUIN1 (**Supplementary Fig. 8**). This observation supports a model where ROQUIN1 dimers are formed following duplex RNA binding.

The capability of wHTH-containing proteins to bind to duplex RNAs at the interface of two monomers has also been described for Zα domain-containing proteins that play a role in antiviral responses by recognizing foreign nucleic acids in the cytoplasm[19]. Its wHTH motif contacts five phosphates of a left-handed duplex Z-RNA with residues from its H3 recognition helix and the W1-loop[13]. Moreover, two Zα domains interact with the RNA duplex without forming a physical dimer, suggesting a cooperative mode of RNA-binding[19].

Discussion

Our work provides insight into the mode of RNA binding by ROQUIN1. Combined structural and biochemical analyses substantiate the involvement of the wHTH motif of the ROQ domain in CDE-containing stem-loop mRNA binding. Furthermore, we illustrate that ROQUIN1 is additionally able to bind to double-stranded RNA and has the potential to be functional in various oligomerization states. Notably, the ROQ domain of ROQUIN1 appears to be sufficient both for RNA binding and dimerization. Finally, we propose a dimer model of the ROQ domain that accounts for stem-loop as well as duplex RNA binding.

During revision of this manuscript, two independent publications appeared describing structural aspects of roquin-RNA interactions[18,20]. The findings of these authors are in general agreement with the data presented here, particularly with regard to the involvement of the wHTH motif in CDE-containing stem-loop RNA binding[18,20], the ability of the ROQ domain to bind also RNA duplexes[18] and to dimerize, either concentration-dependent[20] or induced by duplex RNA binding[18]. The dimeric arrangement seen in the crystal structure of the ROQ domain bound to duplex RNA[18] differs from our proposed dimer model. This difference may be attributed to the use of a different and longer RNA molecule, namely CDE-containing TNF23, in that study compared to the present work. To examine whether our dimer model is also relevant for TNF_{ds} RNA binding, we performed EMSA experiments with the disulfide-stabilized P327C/T258C dimer variant of $RC3H1^{2-452}$ that again displays an increased affinity compared to wild-type protein (**Supplementary Fig. 9a**). Addition of DTT to disrupt disulfide links brings the dsRNA binding affinity back to wild-type level (**Supplementary Fig. 9a**). To rule out unspecific binding of the TNF_{ds} RNA duplex, we finally tested the cysteine-bridged $RC3H1^{2-452}$ dimer for binding of the single-stranded RNA species of TNF_{ds}, which almost abolished binding, indicating the requirement of a duplex nature of the RNA

for efficient binding by ROQUIN1 (**Supplementary Fig. 9b**). Conclusively, multiple modes of interaction with RNA might be possible, depending on the nature of the duplex RNA (see also **Supplementary Fig. 7b**).

Whether the described dimeric states of roquin proteins are physiologically relevant remains to be demonstrated. As indicated by our analytical ultracentrifugation experiments, monomeric ROQUIN1 predominates at lower protein concentrations, but a concentration-dependent dimerization of roquin has been reported by Schlundt *et al.*[20]. Since roquin proteins accumulate in P bodies and stress granules[3,21], it is tempting to speculate that elevated roquin concentration at these sites might favor the formation of functional dimers.

In conclusion, roquin proteins turn out to be very versatile in terms of the secondary structure of their bound RNA targets. It is conceivable that in addition to the reported CDE-containing stem-loop mRNAs also other structure-sequence motifs are recognized within targeted mRNAs, as also indicated by the fact that the majority of the mRNAs enriched in RC3H1 immunoprecipitation experiments were lacking the CDE motif[1]. This opens up exciting prospects for future research, addressing further biological roles of roquin family members.

Methods

Cloning, expression and purification

DNA encoding the RING, ROQ and zf domains of human ROQUIN1 (RC3H1$^{2\text{-}452}$, aa 2-452), the RING and ROQ domains (RC3H1$^{2\text{-}399}$, aa 2-399), the ROQ domain (RC3H1$^{53\text{-}399}$, aa 53-452), and the crystallized ROQ domain (RC3H1$^{178\text{-}328}$, aa 178-328) was subcloned into the pQLinkH vector[22]. The following primers were used for cloning: RC3H1_2fw 5' CAG GAT CCC CTG TAC AAG CTC CAC AAT GG 3', RC3H1_53fw 5' GAG GAT CCG ACC AGA CCA CTA TCA ATA CAG ACA 3', RC3H1_178fw 5' GAG GAT CCC AAC TCT CTT CCA ATC TTT GGG C 3', RC3H1_328rv 5' GAC TGA CTG CGG CCG CTC AGG CTG GAG TCT GCA ACT TG 3', RC3H1_399rv 5' GAC TGA CTG CGG CCG CTC AGC TGT GGT TCT GGA TAT AAT CAA CC 3', and RC3H1_452rv 5' GAC TGA CTG CGG CCG CTC AGC GCT TAT TCA TTT TAC GAA ATT TTT CC 3'. Mutants were generated using the QuikChange Site-Directed Mutagenesis Kit (Stratagene) according to the manufacturer's protocol. The genes were expressed as N-terminal His_7-tagged proteins at 17 °C in *E. coli* Rosetta™ 2 (DE3) (Novagen) using a LEX ultra-high-throughput bench-top bioreactor (Harbinger Biotech). Cells were grown at 37 °C in Terrific Broth medium and induced at an OD_{600} of 2.0-2.5 with 0.5 mM isopropyl β-D-1-thiogalactopyranoside. For purification, cells were resuspended in phosphate-buffered saline (PBS) lysis buffer (1 × PBS pH 7.4, 0.5 M NaCl, 5% (v/v) glycerol, 0.5 mM dithiothreitol (DTT)), supplemented with 0.25% (w/v) 3-[(3-cholamidopropyl)dimethylammonio]-1-propanesulfonate, 0.1 mM phenylmethyl sulfonyl fluoride, 1 U/mL RNase-free DNase I (Qiagen) and one tablet of EDTA-free Complete Protease Inhibitor (Roche). The purification protocol comprises mechanical cell lysis by sonication (SONOPULS HD 2200, Bandelin), Ni/Zn affinity chromatography on a 5 mL HisTrap FF crude column (GE Healthcare), and size-exclusion chromatography on a Superdex 200 prep grade column (XK 26 × 60, GE Healthcare). The His_7 tag was cleaved with tobacco etch virus protease prior to the

gel-filtration step, followed by a reapplication of the cleaved protein on the Ni/Zn affinity column. The purification of protein constructs comprising the RING, ROQ and zf domains additionally included a cation-exchange chromatography on a Source 30S column (HR 16 × 10, GE Healthcare). The P327C/T258C variant was expressed in *E. coli* SHuffle express cells (NEB), and buffers for initial purification steps included 3 mM GSH and 0.6 mM GSSG.

Protein crystallization

The ROQ domain was crystallized using the sitting-drop vapor-diffusion method at 20 °C by mixing equal volumes (200 nL) of His_7-tag cleaved $RC3H1^{2-399}$ or $RC3H1^{53-399}$ protein (8.5 or 10 mg/mL in 20 mM HEPES/NaOH pH 7.5, 0.2 M NaCl, 5 mM DTT, ±1 mM $(NH_4)_2PtCl_4$, respectively) and reservoir solution (Pt derivative: 16% w/v PEG 6000, 10 mM sodium citrate; native: 20% (w/v) PEG 6000, 0.2 M lithium chloride, 0.1 M Tris/HCl pH 8.0, respectively). Before flash-freezing in liquid nitrogen, the crystal was transferred into a cryoprotectant consisting of reservoir solution supplemented with 30% (v/v) glycerol. For derivatization, 0.2 µL 0.5 M $(NH_4)_2PtCl_4$) was added to the crystallization drop before transfer to the cryoprotectant.

Data collection, structure determination and refinement

Diffraction data were collected on BL14.1 operated by the Helmholtz-Zentrum Berlin (HZB) at the BESSY II electron storage ring (Berlin-Adlershof, Germany)[23] at wavelengths of 1.0727 or 0.9184 Å, respectively. Data were processed with the program XDSAPP[24]. Platinum derivative crystals were used for phasing by single-wavelength anomalous diffraction (SAD). Two peak data sets collected from the same crystal were merged with XSCALE[25] to increase multiplicity. The platinum substructure was solved using HKL2MAP[26], and phases derived from the identified platinum positions were used for density modification as implemented in the PHENIX AutoSol wizard[27].

Autobuilding of an initial model and refinement were done with PHENIX[28]. The graphics program COOT[29] was used for model building and visualization. The resulting model was transferred to the high-resolution native data by molecular replacement using the program PHASER[27] and refined with REFMAC[30]. Data collection and refinement statistics are reported in Supplementary Table 1. The Ramachandran map produced by MolProbity[31] shows that 98.7% of the modeled residues are in favored regions with no outliers.

Structure evaluation

Secondary structure elements were assigned using the program DSSP[32]. Searches for similar structures were performed with PDBeFold[8] and the DALI-Server[7]. Interfaces present in the crystal were analyzed using the web service ePISA[17]. Molecular drawings were created with PyMOL Molecular Graphics System (Version 1.3, Schrödinger, LLC). APBS was used for calculating electrostatic surface potentials[33].

Multiple sequence alignment

Amino-acid sequences were aligned using the Clustal Omega server[34], and TEXshade[35] was used for illustration. Uniprot accession numbers are as follows. RC3H1: *Homo sapiens*, Q5TC82; *Mus musculus*, Q4VGL6; *Rattus norvegicus*, D3ZKG8; *Gallus gallus*, E1BZI9; *Xenopus laevis*, Q6NUC6. RC3H2: *Homo sapiens*, Q9HBD1; *Mus musculus*, P0C090; *Rattus norvegicus*, D3ZBM2; *Gallus gallus*, F1NZ02. Roq: *Drosophila melanogaster*, Q9VV48.

Isothermal titration calorimetry

Isothermal titration calorimetry (ITC) measurements were performed at 15 °C in 20 mM Tris/HCl, pH 8.0 and 60 mM KCl using a VP-ITC microcalorimeter (MicroCal Inc.). Prior to the measure-

ment, protein and synthetic RNA (ICOS_13nt: 5'-AUUUC UGUGA AAU-3'; annealed at about 750 μM) were dialyzed against this buffer. Experiments were performed by injecting 55 × 5 μL of 75-100 μM duplex ICOS RNA solution into a sample cell containing 15-20 μM wild-type or P327C/T258C variant of RC3H1$^{2-452}$. Injections were performed with a spacing of 240 s and a reference power of 18 μcal/s. Integration of the injection peaks and construction of binding isotherms was performed by using the high-precision automated peak shape analysis software NITPIC 1.0.3[36]. Data analysis was performed with the Origin 7.0 software (MicroCal, U.S.A) using a one-site binding model.

Analytical gel filtration

Absolute molecular masses of the proteins and RNA complexes were determined by analytical gel filtration using a calibrated 10/300 Superdex 200 column. The running buffer contained 20 mM HEPES/NaOH, pH 7.5 and 0.1 M NaCl. For each protein sample, 50-100 μL of a 1-5 mg/mL protein solution was applied. RNA complexes were prepared by adding the 0.6-fold amount of duplex ICOS_13nt RNA (annealed at about 750 μM) to the protein. The P327C/T258C mutant of RC3H1$^{2-452}$ was analyzed with/without 30 min pre-incubation with 100 mM DTT at room temperature.

Circular dichroism spectroscopy

Wild-type or variant RC3H1$^{2-452}$ proteins were dialyzed against 10 mM sodium phosphate buffer pH 7.5 and 20 mM NaF, and diluted to 2 μM. Spectra were recorded in three replicates at 20 °C from 260 nm to 185 nm, with a 0.1 nm step size using a Chirascan™ CD spectrophotometer (Applied Photophysics Ltd).

Electrophoretic mobility shift assay

The EMSA experiments were performed according to Ryder *et al*.[37] with the following modifications: RNA was prepared by 5′ end-labeling of commercially synthesized RNA oligonucleotides with [γ-^{32}P]-ATP using T4 polynucleotide kinase (NEB). Labeled RNA was gel-purified, eluted and adjusted with water to 0.5 pmol/µL. 350 fmol of labeled RNA was used per 20 µL reaction. Prior to binding reactions, a master mix containing labeled RNA, 1× binding buffer (20 mM Tris-HCl pH 7.5, 50 mM KCl, 5 mM $MgCl_2$, 20 µM $ZnSO_4$, 10% glycerol), 2 mM DTT, and 0.05 mg/ml BSA was heated at 90 °C for 1 min and gradually cooled down to room temperature. In parallel, a dilution series of 10× protein stock was prepared in 1× protein dilution buffer (1× binding buffer, 5 µg/mL heparin). For each binding reaction, 2 µL of the 10× protein stock was added to 18 µL of the master mix at room temperature for 2 to 3 hours. After addition of 4 µL 6× loading buffer (30% glycerol, bromphenol blue, xylene cyanol), RNP complexes were resolved by non-denaturing PAGE (6% polyacrylamide, 0.5× TBE, 5% glycerol) in ice-cold 0.5× TBE buffer containing 20 µM $ZnSO_4$ at 100 V for 40 min. The protein-bound RNA and the free RNA were imaged using a phosphorimager. The P327C/T258C mutant of RC3H1$^{2\text{-}452}$ was analyzed with/without 30 min pre-incubation with 10 mM DTT at room temperature. The results are representative of two to four independent experiments. For K_d calculation, the average of bound fraction from three independent experiments was normalized to the total signal for each lane and plotted against the protein concentration. The data points were fitted by nonlinear regression with errors referring to the standard error of the fit.

Analytical ultracentrifugation

Sedimentation velocity experiments were carried out at 35000 r.p.m. in an XLI analytical ultracentrifuge (Beckman). For all samples 400 µL of RC3H1$^{2\text{-}452}$ protein at a concentration of 0.3 mg/mL ± 1.1-fold excess of stem-loop ICOS RNA (annealed at 2 µM) and reference buffer (20 mM

Hepes pH 7.5, 0.1 M NaCl) were loaded in two-channel center pieces with an optical path length of 12 mm. Samples were measured at 15 °C in an An-50 Ti rotor using the interference optical system. The program SEDNTERP was used to estimate the partial specific volume from amino-acid composition as well as the density ρ and viscosity η of the buffer at 15 °C (http:// bitcwiki.sr.unh.edu/index.php/Main_Page). Data were then analyzed with the program SEDFIT[38] using a continuous c(s) distribution model. Theoretical sedimentation coefficients for monomeric and higher oligomeric protein species were calculated using the following equation

$$s = \frac{\mathrm{M_W}(1\text{-}\rho)}{N_\mathrm{A}(f/f_0)6\pi\eta\sqrt[3]{3\mathrm{M}/\pi N_\mathrm{A}}}$$

with N_A Avogadro's number and $\mathrm{M_W}$ and f/f_0 the protein's molecular weight and frictional ratio, respectively. Assuming a frictional ratio of 1.5, sedimentation coefficients of 2.8, 4.4 and 5.8 or 2.9, 4.6, and 6.1 were calculated for monomeric, dimeric or trimeric uncomplexed protein or protein-RNA complexes, respectively. The monomeric uncomplexed protein has a molecular weight of 50.9 kDa for monomers, the monomeric protein-RNA complex is about 55 kDa.

References

1. Leppek, K. *et al.* Roquin promotes constitutive mRNA decay via a conserved class of stem-loop recognition motifs. *Cell* **153,** 869–881 (2013).
2. Yu, D. *et al.* Roquin represses autoimmunity by limiting inducible T-cell co-stimulator messenger RNA. *Nature* **450,** 299–303 (2007).
3. Glasmacher, E. *et al.* Roquin binds inducible costimulator mRNA and effectors of mRNA decay to induce microRNA-independent post-transcriptional repression. *Nat. Immunol.* **11,** 725–733 (2010).
4. Vogel, K. U. *et al.* Roquin paralogs 1 and 2 redundantly repress the Icos and Ox40 costimulator mRNAs and control follicular helper T cell differentiation. *Immunity* **38,** 655–668 (2013).
5. Pratama, A. *et al.* Roquin-2 shares functions with its paralog Roquin-1 in the repression of mRNAs controlling T follicular helper cells and systemic inflammation. *Immunity* **38,** 669–680 (2013).
6. Harami, G. M., Gyimesi, M. & Kovács, M. From keys to bulldozers: expanding roles for winged helix domains in nucleic-acid-binding proteins. *Trends Biochem. Sci.* **38,** 364–371 (2013).
7. Holm, L. & Rosenström, P. Dali server: conservation mapping in 3D. *Nucleic Acids Res.* **38,** W545–9 (2010).
8. Krissinel, E. & Henrick, K. Secondary-structure matching (SSM), a new tool for fast protein structure alignment in three dimensions. *Acta Crystallogr. D Biol. Crystallogr.* **60,** 2256–2268 (2004).
9. Khayrutdinov, B. I. *et al.* Structure of the Cdt1 C-terminal domain: conservation of the winged helix fold in replication licensing factors. *Protein Sci.* **18,** 2252–2264 (2009).
10. Calabrese, M. F. *et al.* A RING E3-substrate complex poised for ubiquitin-like protein transfer: structural insights into cullin-RING ligases. *Nat. Struct. Mol. Biol.* **18,** 947–949 (2011).
11. Alfano, C. *et al.* Structural analysis of cooperative RNA binding by the La motif and central RRM domain of human La protein. *Nat. Struct. Mol. Biol.* **11,** 323–329 (2004).
12. Yoshizawa, S. *et al.* Structural basis for mRNA recognition by elongation factor SelB. *Nat. Struct. Mol. Biol.* **12,** 198–203 (2005).
13. Placido, D., Brown, B. A., Lowenhaupt, K., Rich, A. & Athanasiadis, A. A left-handed RNA double helix bound by the Z alpha domain of the RNA-editing enzyme ADAR1. *Structure* **15,** 395–404 (2007).
14. Matsumoto, Y. *et al.* Structure of a virulence regulatory factor CvfB reveals a novel winged helix RNA binding module. *Structure* **18,** 537–547 (2010).
15. Anantharaman, V., Zhang, D. & Aravind, L. OST-HTH: a novel predicted RNA-binding domain. *Biol. Direct* **5,** 13 (2010).
16. Soler, N., Fourmy, D. & Yoshizawa, S. Structural insight into a molecular switch in tandem winged-helix motifs from elongation factor SelB. *J. Mol. Biol.* **370,** 728–741 (2007).
17. Krissinel, E. & Henrick, K. Inference of macromolecular assemblies from crystalline state. *J. Mol. Biol.* **372,** 774–797 (2007).
18. Tan, D., Zhou, M., Kiledjian, M. & Tong, L. The ROQ domain of Roquin recognizes mRNA constitutive-decay element and double-stranded RNA. *Nat. Struct. Mol. Biol.* **21,** 679–685 (2014).

19. Athanasiadis, A. Zalpha-domains: at the intersection between RNA editing and innate immunity. *Semin. Cell Dev. Biol.* **23,** 275–280 (2012).
20. Schlundt, A. *et al.* Structural basis for RNA recognition in roquin-mediated post-transcriptional gene regulation. *Nat. Struct. Mol. Biol.* **21,** 671–678 (2014).
21. Athanasopoulos, V. *et al.* The ROQUIN family of proteins localizes to stress granules via the ROQ domain and binds target mRNAs. *FEBS J.* **277,** 2109–2127 (2010).
22. Scheich, C., Kümmel, D., Soumailakakis, D., Heinemann, U. & Büssow, K. Vectors for co-expression of an unrestricted number of proteins. *Nucleic Acids Res.* **35,** e43–e43 (2007).
23. Mueller, U. *et al.* Facilities for macromolecular crystallography at the Helmholtz-Zentrum Berlin. *J. Synchrotron Radiat.* **19,** 442–449 (2012).
24. Krug, M., Weiss, M. S., Heinemann, U. & Mueller, U. XDSAPP: a graphical user interface for the convenient processing of diffraction data using XDS. *J. Appl. Cryst.* **45,** 568–572 (2012).
25. Kabsch, W. XDS. *Acta Crystallogr. D Biol. Crystallogr.* **66,** 125–132 (2010).
26. Pape, T. & Schneider, T. R. HKL2MAP: a graphical user interface for phasing with SHELX programs. *J. Appl. Cryst.* **37,** 843–844 (2004).
27. McCoy, A. J., Grosse-Kunstleve, R. W., Storoni, L. C. & Read, R. J. Likelihood-enhanced fast translation functions. *Acta Crystallogr. D Biol. Crystallogr.* **61,** 458–464 (2005).
28. Adams, P. D. *et al.* PHENIX: a comprehensive Python-based system for macromolecular structure solution. *Acta Crystallogr. D Biol. Crystallogr.* **66,** 213–221 (2010).
29. Emsley, P., Lohkamp, B., Scott, W. G. & Cowtan, K. Features and development of Coot. *Acta Crystallogr. D Biol. Crystallogr.* **66,** 486–501 (2010).
30. Murshudov, G. N., Vagin, A. A. & Dodson, E. J. Refinement of macromolecular structures by the maximum-likelihood method. *Acta Crystallogr. D Biol. Crystallogr.* **53,** 240–255 (1997).
31. Davis, I. W. *et al.* MolProbity: all-atom contacts and structure validation for proteins and nucleic acids. *Nucleic Acids Res.* **35,** W375–83 (2007).
32. Kabsch, W. & Sander, C. Dictionary of protein secondary structure: pattern recognition of hydrogen-bonded and geometrical features. *Biopolymers* **22,** 2577–2637 (1983).
33. Baker, N. A., Sept, D., Joseph, S., Holst, M. J. & McCammon, J. A. Electrostatics of nanosystems: application to microtubules and the ribosome. *Proc. Natl. Acad. Sci. U.S.A.* **98,** 10037–10041 (2001).
34. Sievers, F. *et al.* Fast, scalable generation of high-quality protein multiple sequence alignments using Clustal Omega. *Mol. Syst. Biol.* **7,** 539 (2011).
35. Beitz, E. TEXshade: shading and labeling of multiple sequence alignments using LATEX2 epsilon. *Bioinformatics* **16,** 135–139 (2000).
36. Keller, S. *et al.* High-precision isothermal titration calorimetry with automated peak-shape analysis. *Anal. Chem.* **84,** 5066–5073 (2012).
37. Ryder, S. P., Recht, M. I. & Williamson, J. R. Quantitative analysis of protein-RNA interactions by gel mobility shift. *Methods Mol. Biol.* **488,** 99–115 (2008).
38. Schuck, P. Size-distribution analysis of macromolecules by sedimentation velocity ultracentrifugation and lamm equation modeling. *Biophys. J.* **78,** 1606–1619 (2000).

Acknowledgments

The Protein Sample Production Facility at the Max Delbrück Center is funded by the Helmholtz Association of German Research Centres. The research group of M.L. is funded by the Federal Ministry for Education and Research (BMBF) and the Senate of Berlin, Berlin, Germany. Y.M. is funded by the Deutscher Akademischer Austauschdienst (DAAD). We thank Tracy Dornblut, Janett Tischer and Mandy Mustroph for excellent technical assistance, Kathrin Schulte for supporting the analytical gel filtration measurements, and Michael Krug and Yvette Roske for assistance with diffraction data collection. We acknowledge the beamline support by the staff of the Helmholtz-Zentrum Berlin für Materialien und Energie at BESSY.

Author contributions

A.S. and U.H. designed the study and guided the research experiments. A.S. carried out all the experiments except for EMSA and analytical ultracentrifugation experiments that were performed by Y.M. and E.R., respectively. All authors analyzed data. A.S. wrote and U.H., M.L. and Y.M. revised the manuscript.

Competing financial interests

The authors declare no competing financial interests.

Additional information

Accession codes: Coordinates and structure factors for the ROQ domain of human RC3H1/ROQUIN1 have been deposited in the Protein Data Bank under accession code 4ulw.

Figure legends

Figure 1 Crystal structure of the ROQ domain of ROQUIN1. (**a**) Cartoon model of the overall fold with the wHTH motif highlighted in light blue. (**b**) Topological model of the ROQ domain fold. Coloring in panels a and b is identical. (**c**) The electrostatic surface of the ROQ domain (orientation as in panel a), calculated with the APBS plugin in Pymol (± 5 kT/e; red, negative; blue, positive).

Figure 2 ROQUIN1 stem-loop ICOS-mRNA binding studies. (**a**) EMSA experiments performed with the isolated CDE stem-loop structure of ICOS mRNA and wild-type or variant $RC3H1^{2-452}$. The double mutant corresponds to RK219AA/KR259AA of $RC3H1^{2-452}$. (**b**) Analytical ultra-centrifugation analyses of uncomplexed (—) and stem-loop ICOS RNA-complexed (---) $RC3H1^{2-452}$ protein.

Figure 3 Model of the dimeric ROQ domain, capable to bind to various RNA forms. (**a**) Cartoon model of the dimeric ROQ domain with the wHTH motif highlighted in light blue. Amino acids involved in RNA binding are shown in stick representation. Dimer-stabilizing disulfide bonds, generated by the P327C/T258C mutation, are shown in yellow. (**b**) The electrostatic surface of the dimeric ROQ domain (orientation as in panel a), calculated with the APBS plugin in Pymol (± 5 kT/e; red, negative; blue, positive). (**c**) EMSA performed with the P327C/T258C variant of the $RC3H1^{2-452}$ protein and the isolated CDE stem-loop structure of ICOS mRNA. (**d**) ITC isotherms characterizing the binding of wild-type and P327C/T258C $RC3H1^{2-452}$ protein to duplex ICOS RNA. The data were fitted to a one-site binding model, revealing K_d values of 68.9 ± 8.6 nM and 724.6 ± 20.9 nM and stoichiometry values of n=0.499 ± 0.003 and n=0.469 ± 0.002 for wild-type and cysteine-bridged dimer of $RC3H1^{2-452}$, respectively, with errors referring to the standard error of the fit.

Tables

Table 1 Data collection, phasing and refinement statistics.

	RC3H1$^{178-328}$ Pt derivative	RC3H1$^{177-328}$ native
Data collection		
Space group	$P2_12_12$	C2
Cell dimensions		
a, *b*, *c* (Å)	61.3, 160.5, 29.4	169.7, 29.8, 60.2
α, β, γ (°)	90, 90, 90	90, 100.9, 90
Resolution (Å)	40.31-2.17 (2.25-2.17)	44.39-1.91 (1.98-1.91) *
R_{merge} (%)	8.9 (52.5)	9.5 (44.3)
$< I / \sigma(I) >$	14.7 (2.8)	9.1 (2.0)
Completeness (%)	98.9 (91.3)	99.2 (95.7)
Redundancy	7.3 (4.4)	3.2 (2.9)
Refinement		
Resolution (Å)	2.17	1.91
No. reflections	117,110	75,166
R_{work} / R_{free} (%)		20.0 / 24.1
No. atoms		2,564
Protein		2,403
Water		161
Average B-factor (Å²)		
Overall		25.8
Protein		25.6
Water		29.0
R.m.s deviations		
Bond lengths (Å)		0.016
Bond angles (º)		1.56

*Highest resolution shell is shown in parenthesis.
One single crystal was used to collect a complete dataset for each structure.

Figure 1

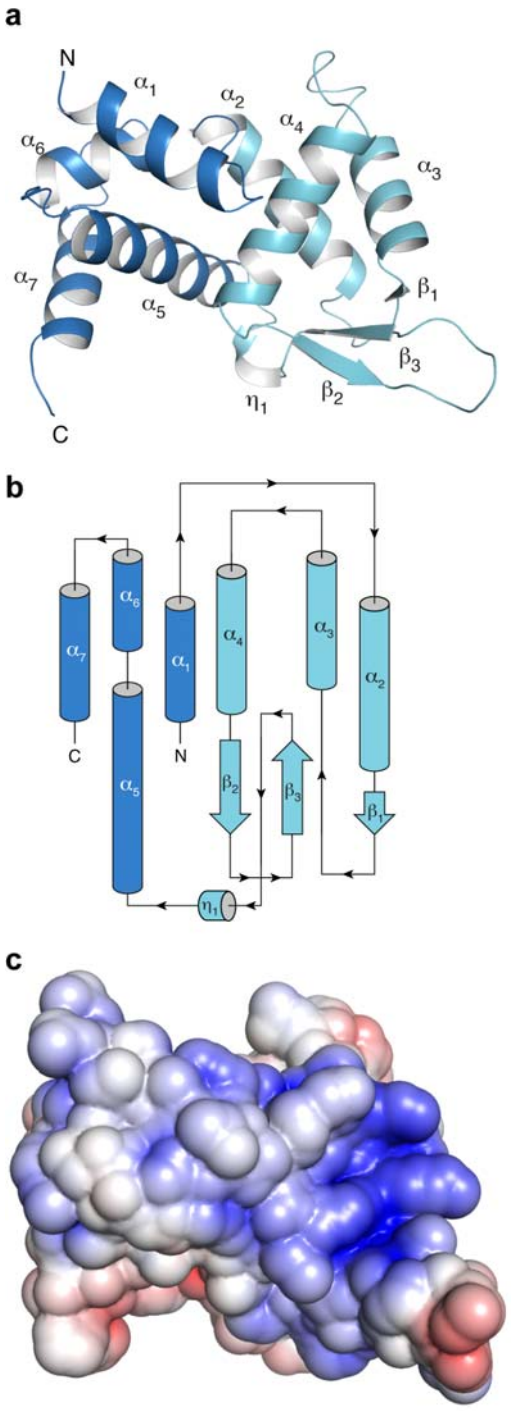
a
N
α1
α2
α4
α6
α3
α7
α5
β1
β3
β2
η1
C
b
α6
α7
α1
α4
α3
α2
C
N
α5
β2
β3
β1
η1
c

Figure 2

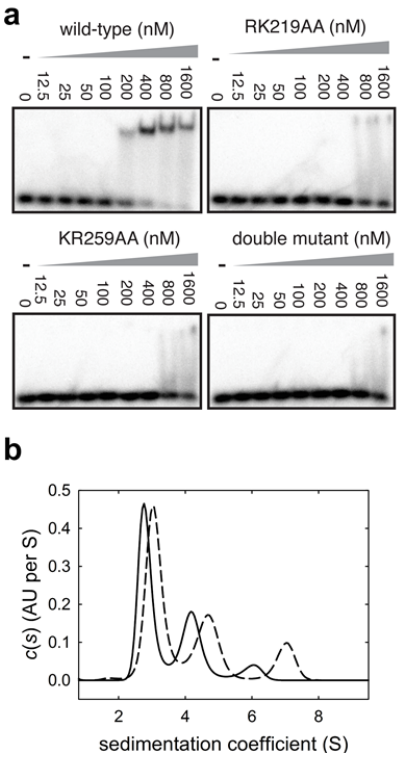
a
wild-type (nM)
RK219AA (nM)
KR259AA (nM)
double mutant (nM)
-
0
12.5
25
50
100
200
400
800
1600
b
c(s) (AU per S)
0.0
0.1
0.2
0.3
0.4
0.5
2
4
6
8
sedimentation coefficient (S)

Figure 3

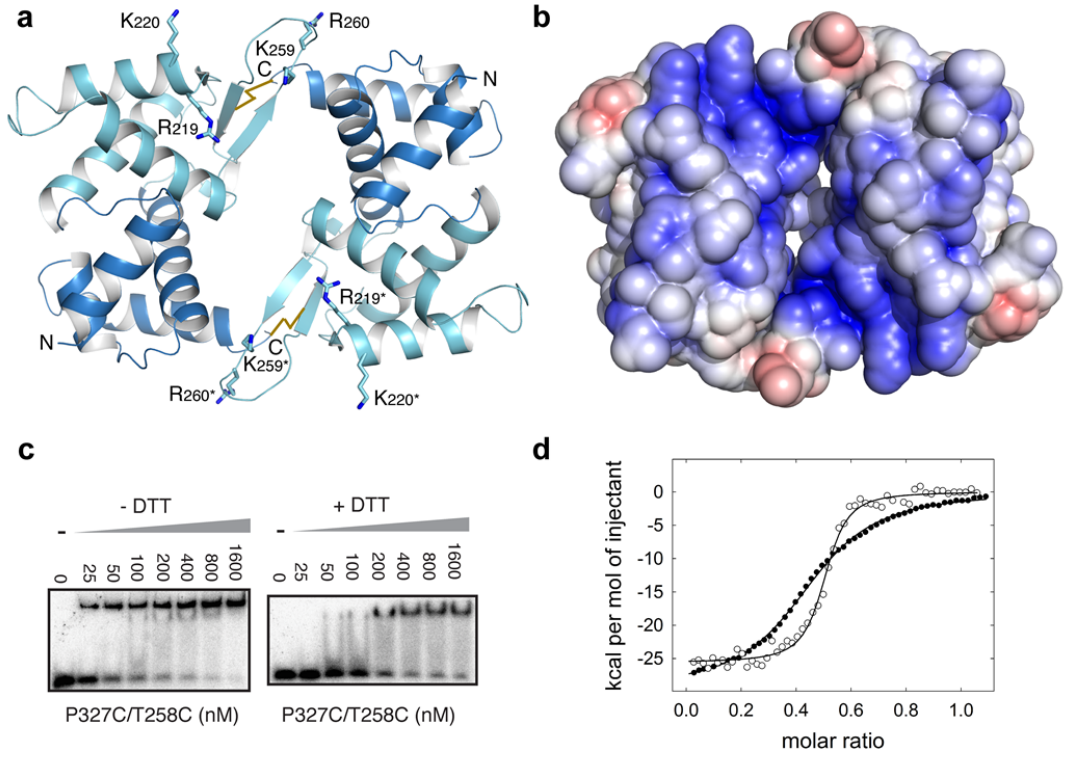
a
K220
R260
K259
C
N
R219
R219*
N
C
K259*
R260*
K220*
b
c
- DTT
+ DTT
-
0
25
50
100
200
400
800
1600
P327C/T258C (nM)
P327C/T258C (nM)
d
kcal per mol of injectant
0
-5
-10
-15
-20
-25
0.0
0.2
0.4
0.6
0.8
1.0
molar ratio